COMPUTER SIMULATION OF THE FLOW IN THE ABDOMINAL ANEURYSMATIC AORTA

Z. Tonar*, J. Jeník*, V. Třeška** and M. Novák**

* University of West Bohemia/Department of Mechanics, Pilsen, Czech Republic
** University Hospital/Department of Surgery, Pilsen, Czech Republic
*** University Hospital/Radiodiagnostic Clinic, Pilsen, Czech Republic

tonar@ntc.zcu.cz

Abstract: Our aim was to develop a computer model of the blood flow and vascular wall mechanics in the descending abdominal aneurysmatic aorta. The purpose was to study the relationship between the flow structure, wall behaviour, and aneurysm morphology. Morphology of a realistic model of the aortic lumen was based on a data obtained from a 76-year-old male patient undergoing computer tomography of descendent aorta and pelvic arteries. The geometry was created and covered with surface mesh in the *Amira*^{TM} software. The numerical simulation was performed in the *Fluent* software. The numerical model was based on the equation of mass conservation with constant value of density and on the system of Navier-Stokes equations. The constitutive relations represented the Newtonian fluid. The inlet boundary condition was represented by the pulsatile flow. The outlet boundary condition was the pressure outlet (1.10^5 *Pa* in each of the iliac arteries). The lumen of arteries was modelled as encircled by a rigid wall and the fluid-wall interaction was taken into account. The discretisation was realized by finite element method. Collections of maps were obtained describing redistribution of the wall stress contours and the velocity profiles.

Introduction

Numerical simulation of the flow in the aortic system proved itself to be a promising method for better understanding of the development of atherosclerotic abdominal aortic aneurysm (AAA) and its dependence on flow structure [1]. Our first task was to create a simplified finite-element grid of the lumen of aneurysmatic aorta and its main visceral and pelvic branches. The second aim was to study the blood flow through this realistic geometry, taking into consideration the interaction of the fluid with the vessel wall.

Interaction between a fluid and a solid continuum

A loosely coupled method of interaction is useful for the solution of the interaction between a fluid and a solid continuum. This method is based on an alternately separated solution of both the fluid and the solid phase. The interface between fluid and solid part is composed of appropriate boundary conditions shared by both phases. The boundary is updated during each of the time steps. The basic algorithm is built up on two steps. The first one represents a solution of the fluid part where the vessel wall rigidity is taken in consideration. This configuration is signed as initial undeformed configuration and the first step produces the pressure field on the shared boundary condition. The second step represents a solution of elastic solid phase loaded by pressure field on its shared interface. Thereby the fluid channel becomes deformed and it is necessary to repair the solution of the fluid part where the solid wall rigidity is again taken into consideration. These steps are being solved up to limitation of convergency.

Materials and Methods

The morphology of the computational 3-D tetrahedral grid was obtained from 76-year-old male patient undergoing computer tomography (CT) angiography of descendent aorta and pelvic arteries because of subrenal abdominal aortic aneurysm (AAA, length of 14.5 cm, width 8 cm, parietal thrombus 4 cm thick; inner diameter of aneurysm was 57 mm $\times$ 41 mm), affecting also both of the common iliac arteries. The data were transferred from a 16-row CT (Somatom Sensation 16, Siemens, Forchheim, Germany) via the DICOM format into Amira^{TM} 3.1.1 software (TGS Europe, Merignac Cedex, France), see Fig. 1. Full spatial resolution of the CT data matrix was preserved (512 pixels $\times$ 512 pixels, nominal slice thickness (collimation) of 0.75 mm, increment of 0.75 mm). The calibrated image data set was segmented semiautonomically with respect to the lumen of aorta. Neither visceral nor parietal branches of aorta were considered. The quality of the grid (23.000 tetrahedral elements) was enhanced by adaptive resizing of elements according to vessel diameter and irregular regional shape of the aneurysm (Gambit, Fluent Europe, Sheffield, Great Britain).

Computer simulation of the fluid continuum by means of the finite element volume (FEV) method

The numerical simulation was performed with use of the commercial software *Fluent* (Fluent.Inc Europe). The computations started with simulation of simple steady laminar flow with constant values of density and

ISSN: 1727-1983

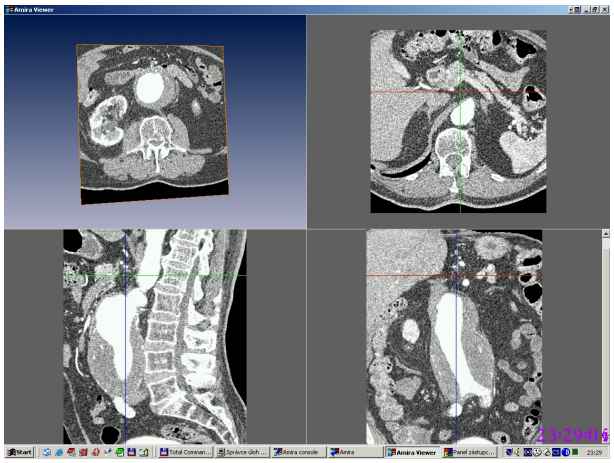

Figure 1: CT-angiography, four-view.

kinematic viscosity. The model was then improved, i.e. we proceeded to the modelling of an unsteady flow, where the non-constant value of viscosity depended on the shear rate. The power law model was used for this purpose. For the first approach, we took into account the laminar flow of Newtonian fluid with constant value of density $\rho = 1050\ (kg \cdot m^{-3})$ and constant value of the dynamic viscosity given by value of kinematic viscosity $\nu = 0.0042\ (m \cdot s^{-2})$. For this purpose, we used the equations of mass conservation

$$\frac{\partial \rho}{\partial t} + \frac{\partial}{\partial y_i}(\rho v_i) = 0, \tag{1}$$

where ρ represent density and v_i velocity of the fluid stream, and the system of Navier-Stokes equations for incompressible continuum

$$\frac{\partial p}{\partial y_j} - \eta \frac{\partial}{\partial y_j}\left(\frac{\partial v_i}{\partial y_j}\right) = \rho f_i - \rho \frac{Dv_i}{Dt}. \tag{2}$$

The second term on the right side of equation 2 represented the material derivation of an appropriate quantity. To obtain this form of Navier-Stokes equations, we started with the equation of force conservation

$$\rho \frac{Dv_i}{Dt} = \rho f_i + \frac{\partial \tau_{ij}}{\partial y_j}. \tag{3}$$

We put the the constitutive relation for the stress tensor τ_{ij} into the equation 3

$$\tau_{ij} = -p\delta_{ij} + R_{ij}, \tag{4}$$

where p stood for the pressure, δ_{ij} for the Kronecker delta and R_{ij} for the dissipation tensor

$$R_{ij} = 2\eta \dot{e}_{ij} + \acute{\eta} \dot{e}_{ll} \delta_{ll}, \tag{5}$$

where η denotes dynamic viscosity and $\acute{\eta}$ the so-called second viscosity. The tensor of strain rate $\dot{e}_{ij}$ is given by kinematic relation

$$D_{ij} = \dot{e}_{ij} = \frac{1}{2}\left(\frac{\partial v_j}{\partial y_i} + \frac{\partial v_i}{\partial y_j}\right). \tag{6}$$

Pulsatile velocity boundary condition

The inlet boundary condition of continuum flow was represented by the pulsatile velocity profile, which was called *velocity inlet* in terminology of the software package Fluent [2]. The theory of oscillatory pulsatile flow was described in [3]. This theory is based on the system of Navier-Stokes equations for unsteady viscous incompressible continuum

$$\frac{\partial^2 w_p}{\partial r^2} + \frac{1}{r}\frac{\partial w_p}{\partial r} - \frac{1}{\nu}\frac{\partial w_p}{\partial t} = \frac{1}{\eta}\frac{\partial p}{\partial x}, \tag{7}$$

where the velocity boundary condition of the wall was set to $w_p = 0$ and the inner radius $r = R$ was taken into account. The evolution of the pressure gradient in time was used as a periodic function of time and therefore it was useful to put the development in Fourier series form

$$-\frac{\partial p}{\partial x} = Re\left[\sum_{n=0}^{\infty} A\, e^{i(n\omega_0 t + \phi_n)}\right], \tag{8}$$

where base frequency was signed as ω_0, amplitude as A, and n was the sequence of harmonic components. *Re* stood for the real part of complex value in the square brackets. For $n = 1,\ \phi_1 = \phi,\ \omega_0 = \omega$ we wrote

$$-\frac{\partial p}{\partial x} = Re\left[A e^{i(\omega t + \phi)}\right]. \tag{9}$$

Finally, using the equations above, we converted the expression 7 into the following relation

$$\frac{\partial^2 w_p}{\partial r^2} + \frac{1}{r}\frac{\partial w_p}{\partial r} - \frac{1}{\nu}\frac{\partial w_p}{\partial t} = \frac{A}{\eta} e^{i\omega t}. \tag{10}$$

This form of Navier-Stokes equations lead to Bessel zero-order equation so we were allowed to deduce the following form

$$w_p = Re\left\{\frac{AR^2}{\eta}\frac{1}{\alpha^2 i^3}\left[1 - \frac{J_0\left(\alpha y i^{3/2}\right)}{J_0\left(\alpha i^{3/2}\right)}\right] e^{i\omega t}\right\}, \tag{11}$$

where $y = r/R$ denoted the relative radius, $\alpha = R\sqrt{\omega/\nu}$ stood for a frequency parameter also called the Womersley number, where R was the radius of the tube (i.e. vessel wall), η was the dynamic viscosity and ω defined the angular velocity.

The solution of the Bessel function was built up on the solution of Kelvin function [4] for the equation

$$x^2 y'' + xy' - ix^2 y = 0. \tag{12}$$

The common integral of this term was

$$y = c_1 J_0\left(i^{3/2}x\right) + c_2 K_0\left(i^{1/2}x\right). \tag{13}$$

Function $J_0\left(i^{3/2}x\right)$ was developed into series

$$J_0\left(i^{3/2}x\right) = 1 + i\frac{\left(\frac{x}{2}\right)^2}{(1!)^2} - \frac{\left(\frac{x}{2}\right)^4}{(2!)^2} - i\frac{\left(\frac{x}{2}\right)^6}{(3!)^2}\ldots \tag{14}$$

ISSN: 1727-1983

and therefore we were allowed to put

$$J_0\left(i^{3/2}x\right) = ber\,x + i\,bei\,x, \tag{15}$$

where function 16 and 17 were referred as Kelvin function–Bessel real $ber\,x$ and Bessel imaginary $bei\,x$ of the function J_0.

$$ber\,x = 1 - \frac{\left(\frac{x}{2}\right)^4}{(2!)^2} + \frac{\left(\frac{x}{2}\right)^8}{(4!)^2} - \frac{\left(\frac{x}{2}\right)^{12}}{(6!)^2}\ldots \tag{16}$$

$$bei\,x = \frac{\left(\frac{x}{2}\right)^2}{(1!)^2} - \frac{\left(\frac{x}{2}\right)^6}{(3!)^2} + \frac{\left(\frac{x}{2}\right)^{10}}{(5!)^2}\ldots \tag{17}$$

The stationary component of the velocity was defined by the relation

$$w_s = -\frac{q_s R^2}{4\eta}\left(1-y^2\right), \tag{18}$$

where q_s was stationary component of the final pressure gradient which was build by stationary and pulsatile component $\frac{dp}{dx} = q = q_s + q_p$. The final pulsatile velocity in the tube was composed by the stationary velocity and by the pulsatile velocity component of the flow, as shown by the following relation

$$w = w_s + w_p. \tag{19}$$

Figure 2 presents the development of velocity profiles during the periodic time cycle for Womersley number $\alpha = 21(-)$.

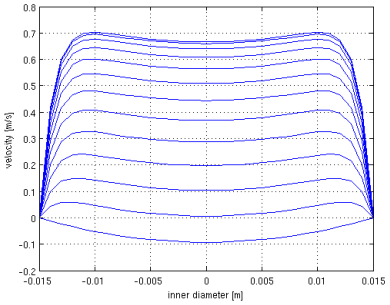

Figure 2: Pulsatile velocity inlet boundary condition during a periodic time cycle.

Presenting the boundary condition of the fluid part of the model, we have to mention also the outlet boundary condition. It was simply represented by a constant pressure of 1.10^5 *Pa* in each of the iliac arteries, as adopted from expert literature [5]. This kind of conditions were named *pressure outlet* in the Fluent environment.

Mathematical model of the solid continuum FEM

The mathematical simulation of solid part was based on the finite element method (FEM). The system showed the behaviour of a deforming body where an isotropic, linear, homogeneous material (described by constitutive relation well known as Hook's theorem) was taken into account. The real field of movements inside the mesh of tetrahedral elements was replaced by linear base functions

$$\begin{aligned} u &= \alpha_1 + \alpha_2\,x + \alpha_3\,y + \alpha_4\,z \\ v &= \alpha_5 + \alpha_6\,x + \alpha_7\,y + \alpha_8\,z \\ w &= \alpha_9 + \alpha_{10}\,x + \alpha_{11}\,y + \alpha_{12}\,z. \end{aligned} \tag{20}$$

The field of movements was continuous. The density of deformation energy of the isotropic homogenous material, where the behaviour according the Hook's law was expected, was given by the term

$$\Lambda = \frac{1}{2}\left(\sigma_x\varepsilon_x + \sigma_y\varepsilon_y + \sigma_z\varepsilon_z + \tau_{xy}\gamma_{xy} + \tau_{yz}\gamma_{yz} + \tau_{zx}\gamma_{zx}\right), \tag{21}$$

where σ defined the main tension, ε was relative extension and τ signed the shear stress. Hook's law could be expressed in a matrix form

$$\sigma = E\cdot\varepsilon, \tag{22}$$

and the matrix of the elastic constants E [6] was in the following form

$$E = \frac{E\cdot(1-\mu)}{(1+\mu)\cdot(1-2\mu)}\cdot \begin{bmatrix} 1 & \frac{\mu}{1-\mu} & \frac{\mu}{1-\mu} & 0 & 0 & 0 \\ \frac{\mu}{1-\mu} & 1 & \frac{\mu}{1-\mu} & 0 & 0 & 0 \\ \frac{\mu}{1-\mu} & \frac{\mu}{1-\mu} & 1 & 0 & 0 & 0 \\ 0 & 0 & 0 & \frac{1-2\mu}{2\cdot(1-\mu)} & 0 & 0 \\ 0 & 0 & 0 & 0 & \frac{1-2\mu}{2\cdot(1-\mu)} & 0 \\ 0 & 0 & 0 & 0 & 0 & \frac{1-2\mu}{2\cdot(1-\mu)} \end{bmatrix} \tag{23}$$

and finally ε was the vector of appropriate relative extensions. The values were adopted according to [7] so the wall Young's modulus was set to $E = 2.5MPa$ and Poisson coefficient was set to $\mu = 0.45$ (nearly incompressible material). We were allowed to express the density of deformation energy by the equation

$$\Lambda = \frac{1}{2}\cdot\varepsilon^T\cdot E\cdot\varepsilon. \tag{24}$$

The vector ε was given by Cauchy's form

$$\varepsilon_{kl} = \frac{1}{2}\left(\frac{\partial u_k}{\partial x_l} + \frac{\partial u_l}{\partial x_k}\right) \tag{25}$$

Deformation energy of a tetrahedral element was given by integrating the density of deformation energy through the volume of the element. Applying the stiffness matrix of the mesh element, the deformation energy was expressed.

The surface boundary condition represented a force loading the appropriate surface. The directions of the loading pressure vector were obtained by right-hand rules in directions of the increasing nodes indices (the vector of right sides in FEM terminology); in fact, it was the vector of force component relevant to each of the nodes

$$f_c = \begin{bmatrix} f_1^T & f_2^T & f_3^T & \ldots & f_{N_p}^T \end{bmatrix}^T. \tag{26}$$

ISSN: 1727-1983

Figure 3: Anterior view on the lumen with subrenal aneurysm. The visceral branches of aorta were not involved in the simulation.

The global stiffness matrix covered the system of relations among all the nodal movements represented by vector Δ_c and appropriate components of nodal reactions forces. These reactions forces had to be in balance with the outer force field.

$$\Delta_c = \left[\begin{array}{ccccc} \Delta_1^T & \Delta_2^T & \Delta_3^T & \ldots & \Delta_{N_p}^T \end{array} \right]^T. \qquad (27)$$

This balance was expressed with the term

$$K_c \cdot \Delta_c = f_c. \qquad (28)$$

With knowing the node movements, it was possible to express the spatial tensions according to Von Mises (HMH) method, as shown by the following expression

$$\sigma_{red_{HMH}} = \frac{1}{\sqrt{2}} \cdot \cdot \sqrt{(\sigma_x - \sigma_y)^2 + (\sigma_y - \sigma_z)^2 + (\sigma_z - \sigma_x)^2 + 6 \cdot (\tau_{xy}^2 + \tau_{yz}^2 + \tau_{zx}^2)}. \qquad (29)$$

Results

The developed model (Fig. 3) reflected the most significant features of the vessel wall altered by atherosclerosis and asymmetric aneurysmatic dilatation. The model included huge and medium-sized vessels, with mesh density created adaptively according to the lumen. During the systole, two swirls developed ventrally in the cranial segment of aneurysm and laterally in the right junction of aneurysm neck and sac close to the origin of right renal artery. Both swirls persisted through the whole cardiac cycle with maximum in end-diastolic phase. The distribution pattern of stress contours according to Von Mises HMH method was computed (Fig. 4). The highest stress values were found in the left dorsal part of the cranial third of the aneurysm. The velocity vectors during the whole cardiac cycle were computed (Fig. 5).

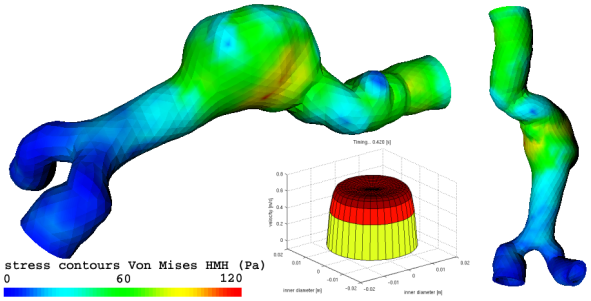

Figure 4: Stress contours at systolic peak, left lateral view and dorsal view.

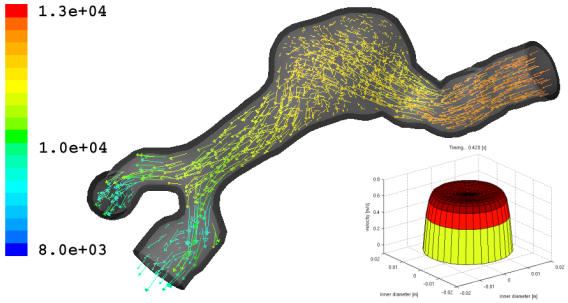

Figure 5: Velocity vectors coloured by static pressure at systolic peak, left lateral view.

Discussion

During the computation, we found the spatial resolution of the model to be sufficient even in the very irregular and realistic morphology of the aneurysm. The lateral swirl could be caused by the effect of local irregular bending of aneurysm neck. In our case of realistic model, the swirls persisted through both systole and diastole. In an idealised smooth model of AAA without branching [1], the whirls regressed during the peak systolic flow and (unlike in our model) other swirls originated in the caudal segment of AAA. Our simulation of distribution pattern of stress contours in the wall of the aneurysmatic sac yielded heterogeneous values comparable to [7, 8], with maximum in the dorsal part of the cranial third of the aneurysm. As the hemodynamic parameters of the patient under study were not included in the model, the results do not provide the actual wall stresses of this patient – they provide information on the stress pattern and rather characterise the geometrical type of the aneurysm. Unlike Di Martino et al. [7], we did not observe any significant vessel wall displacement. The reason is that in our simulation, the reference configuration of the wall model was set after processing the very first cardiac cycle. Although the simulation was performed for the Newtonian fluid only, we would have expected tiny differences in flow structure between results based on Newtonian and non-Newtonian fluid, as our model comprised no small vessels.

The 3-D flow field in AAA depends a great deal on the geometry of the vessel, as proved by simulations of flow pattern in hypothetically shaped idealized and asym-

ISSN: 1727-1983

metric models under realistic pulsatile flow conditions [9, 10]. However, simple geometric criteria are unreliable in modelling AAA biomechanics and the potential for rupture of an individual AAA can not be estimated in simulations based on statistics from aggregate populations [11]. In realistic models involving abdominal aortic branches, more information on the flow field in bifurcation regions can be acquired. Such information may provide an additional insight into hemodynamic factors involved in the predilection of atherosclerotic lesions in AAA development [12]. When modelling vascular networks with multiple branches, outflow boundary conditions play a great role in blood flow distribution. Also the effect of exercise on hemodynamic conditions and flow redistribution in aorta is considerable [13].

Patients with AAA are in danger of aneurysm rupture, which occurs most often in dorsal or dorsolateral wall of the aneurysmatic sac. Morphological and mechanical risk factors of rupture include e.g. aneurysm diameter and its expansion rate, loss of elastin and inflammatory infiltrates leading to mechanical inferiority of the wall, tensile wall stress, shear stress, flow patterns and swirls, blood pressure, etc. [14]. We did not solve the wall shear stress problem, as under common conditions the physiologic shear stress on the inner wall is of lesser effect than the tensile stress within the wall due to pressure in an AAA [15]. Simulation of aneurysm fluid dynamics and its effect on aneurysm wall mechanics in realistic 3-D models [7] served already as a guidance to assess the risk of rupture of the aneurysm. Similar to our study, the authors delt with the aneurysmatic sac only, omitting the hemodynamic influence of arterial branches of precedent and subsequent segment of the aorta. However, the effect of the flow in aorta branches on the flow in the aneurysm might be significant and deserves a further interest.

Fillinger [15] analysed rupture risk over time in patients with AAA under observation, performing nonlinear hyperelastic modelling of aneurysm wall behaviour compared to CT data and blood pressure observation. A noninvasive study of 3-D tensile wall stress was found to be superior to maximum diameter for determining rupture risk. The simulation of wall stress provided significant differences of clinical use for aneurysms that could be safely observed for longer periods or needed surgical repair to prevent rupture within a short time. The effect of 3-D shape appeared to dominate the effect of blood pressure and the influence of diameter. Asymmetry and wall thickness on stresses has been studied thoroughly in both theoretical and CT-based realistic 3-D models of AAA [16, 17].

At present, there is need for predictive models with realistic morphology in order to gather experience with computational simulations correlated to clinical decision making. Our method of finite-element grid construction enables us to consolidate the view of clinical medicine (i.e. vascular surgery), diagnostic imaging methods and computational simulation. It does not describe the very important composition of atherosclerotic vessel wall and of intraluminal thrombus, which can be extracted from high-resolution magnetic resonance [18]. Nevertheless, CT angiography remains the most frequent and routine method of aneurysm diagnostics and morphometry in patients undergoing elective surgery for this condition.

Young healthy patients with large aneurysms have a risk-benefit ratio that favours vascular or endovascular surgery. The presented method could be useful in patients with boundary value of aneurysm diameter and high surgical risk or in asymptomatic patients with smaller aneurysms (5–6 cm) without rapid expansion. In these patients, the final decision on surgery could be ambiguous because mortality and morbidity of elective surgery are too high when compared to conservative treatment. Also the tensile stress analysis of the aneurysm wall has the potential to aid management in patients who are at high risk for surgery and have aneurysms of a moderate size [15]. Pulsatile flow assessment should help the surgeon to evaluate localisation and significance of swirls in the AAA. Whether simulation of wall shear stress correlates with the risk of initial dissection of AAA, remains unsolved. Until now, we are lacking reference papers and case-reports bringing clinical experience with complementary results of simulation of blood flow through the AAA of the same patient. Our prospective work will be focused on the redistribution of the wall stress on the non-rigid wall induced by flow structure.

Conclusions

Creating mathematical models based on real morphology provides a tool integrating the view of medical diagnostics, therapy, and modelling of AAA. The numerical results obtained in this study showed the flow features and wall stress distribution in a model of AAA with realistic morphology. The approach presented was found to be suitable e.g. for follow-up study of patients observed for the aneurysm growth, where simulations could be correlated with surgeon's clinical experience. Then modelling of blood flow characteristics could be considered properly when predicting the individual aneurysm rupture potential.

Acknowledgements

This work was supported by the project MSM 4977751303 awarded by the Ministry of Education, Youth and Sports of the Czech Republic.

References

[1] FINOL, E. A., KEYHANI, K., and AMON, C. H. The effect of asymmetry in abdominal aortic aneurysms under physiologically realistic pulsatile flow conditions. *J. Biomech. Eng.*, 125:207–217, 2003.

[2] FLUENT INC. EUROPE Sheffield, Great Britain. Fluent 6.1. manual, 2001.

ISSN: 1727-1983

[3] VALENTA, J. Biomechanics. Academia, Prague, 1985.

[4] REKTORYS, K. Přehled užité matematiky 1 [outlines of applied mathematics vol. 1]. Prometheus, Prague, 1995.

[5] MILLS, C. J., GABE, I. T., GAULT, J. H., MASON, D. T., ROSS JR., J., BRAUNWALD, E., and SHILLINGFORD, J. P. Pressure-flow relationships and vascular impedance in man. *Cardiovascular Research*, 4:405–417, 1970.

[6] BATHE, K. J. Finite element procedures. *Prentice-Hall, Inc., New Jersey, pp. 194*, 1996.

[7] DI MARTINO, E. S., GUADAGNI, G., FUMERO, A., BALLERINI, G., SPIRITO, R., BIGLIOLI, P., and REDAELLI, A. Fluid-structure interaction within realistic three-dimensional models of the aneurysmatic aorta as a guidance to assess the risk of rupture of the aneurysm. *Med. Eng. Phys.*, 23:647–655, 2001.

[8] LEE, D. and CHEN, J. Y. Numerical simulation of steady flow fields in a model of abdominal aorta with its peripheral branches. *J. Biomech.*, 35:1115–1122, 2002.

[9] FINOL, E. A. and AMON, C. H. Flow-induced wall shear stress in abdominal aortic aneurysms: Part ii – pulsatile flow hemodynamics. *Comput. Methods Biomech. Biomed. Engin.*, 5:319–328, 2002.

[10] YIP, T. H. and YU, S. C. M. Cyclic flow characteristics in an idealized asymmetric abdominal aortic aneurysm model. *Proc. Inst. Mech. Eng.*, 217:27–39, 2003.

[11] HUA, J. and MOWER, W. R. Simple geometric characteristics fail to reliably predict abdominal aortic aneurysm wall stresses. *J. Vasc. Surg.*, 34:308–315, 2001.

[12] SHIPKOWITZ, T., RODBERS, V. G. J., FRAZIN L. J., and CHANDRAN, K. B. Numerical study on the effect of secondary flow in the human aorta on local shear stresses in abdominal aortic branches. *J. Biomech.*, 33:717–728, 2000.

[13] TAYLOR, C. A., HUGHES, T. J. R., and ZARINS, C. K. Effect of exercise on hemodynamic conditions in the abdominal aorta. *J. Vasc. Surg.*, 29:1077–1089, 1999.

[14] SONESSON, B., SANDGREN, T., and LANNE, T. Abdominal aortic aneurysm wall mechanics and their relation to risk of rupture. *Eur. J. Vasc. Endovasc. Surg.*, 18:487–493, 1999.

[15] FILLINGER, M. F., MARRA, S. P., RAGHAVAN, M. L., and KENNEDY, F. E. Prediction of rupture risk in abdominal aortic aneurysm during observation: Wall stress versus diameter. *J. Vasc. Surg.*, 37:724–732, 2003.

[16] RAGHAVAN, M. L., VORP, D. A., FEDERLE, M. P., MAKAROUN, M. S., and WEBSTER, M.W. Wall stress distribution on three-dimensionally reconstructed models of human abdominal aortic aneurysm. *J. Vasc. Surg.*, 31:760–769, 2000.

[17] THUBRIKAR, M. J., AL-SOUDI, J., and ROBICSEK, F. Wall stress studies of abdominal aortic aneurysm in a clinical model. *Ann. Vasc. Surg.*, 15:355–366, 2001.

[18] YANG, F., HOLZAPFEL, G., SCHULZE-BAUER, C., Stollberger, R., THEDNS, D., BOLINGER, L., STOLPEN, A., and SONKA, M. Segmentation of wall and plaque in in vitro vascular mr images. *Int. J. Cardiovasc. Imaging*, 19:419–428, 2003.

ISSN: 1727-1983